X-ray Raman spectroscopy of lithium-ion battery electrolyte solutions in a flow cell

Didem Ketenoglu,[a]* Georg Spiekermann,[b] Manuel Harder,[c] Erdinc Oz,[d,e,c] Cevriye Koz,[f] Mehmet C. Yagci,[g] Eda Yilmaz,[h] Zhong Yin,[c,i,j] Christoph J. Sahle,[k] Blanka Detlefs[k] and Hasan Yavaş[c]

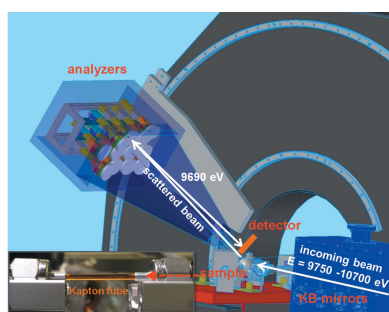[a]Department of Engineering Physics, Faculty of Engineering, Ankara University, Ankara 06100, Turkey, [b]Institute of Earth and Environmental Science, University of Potsdam, Potsdam 14476, Germany, [c]Deutsches Elektronen-Synchrotron DESY, Hamburg 22607, Germany, [d]Science and Art Faculty, Physics Department, Inonu University, Malatya 44280, Turkey, [e]Institute of Accelerator Technologies, Ankara University, Ankara 06830, Turkey, [f]Department of Physics, Stephenson Institute for Renewable Energy, University of Liverpool, Liverpool L69 7ZE, UK, [g]Institute of Energy Systems Technology (INES), Offenburg University of Applied Sciences, Offenburg 77652, Germany, [h]National Nanotechnology Research Center and Institute of Materials Science and Nanotechnology (UNAM), Bilkent University, 06800 Ankara, Turkey, [i]Max Planck Institute for Biophysical Chemistry, Göttingen 37077, Germany, [j]Laboratory for Physical Chemistry, ETH Zurich, Zurich 8092, Switzerland, and [k]European Synchrotron Radiation Facility, Grenoble 38043, France. *Correspondence e-mail: dketen@eng.ankara.edu.tr

The effects of varying $LiPF_6$ salt concentration and the presence of lithium bis(oxalate)borate additive on the electronic structure of commonly used lithium-ion battery electrolyte solvents (ethylene carbonate–dimethyl carbonate and propylene carbonate) have been investigated. X-ray Raman scattering spectroscopy (a non-resonant inelastic X-ray scattering method) was utilized together with a closed-circle flow cell. Carbon and oxygen K-edges provide characteristic information on the electronic structure of the electrolyte solutions, which are sensitive to local chemistry. Higher Li^+ ion concentration in the solvent manifests itself as a blue-shift of both the π^* feature in the carbon edge and the carbonyl π^* feature in the oxygen edge. While these oxygen K-edge results agree with previous soft X-ray absorption studies on $LiBF_4$ salt concentration in propylene carbonate, carbon K-edge spectra reveal a shift in energy, which can be explained with differing ionic conductivities of the electrolyte solutions.

1. Introduction

High-performance energy storage systems are at the heart of modern sustainable energy applications. Among the commercially available electrochemical energy storage systems, lithium-ion batteries (LIBs) are one of the most widely used devices. Due to their relatively high energy density, LIBs are particularly preferred for portable electronics and electric vehicles; more recently they are becoming a viable alternative for grid storage as well (Dunn *et al.*, 2011; Yuan *et al.*, 2011; Ehrlich, 2002; Armand & Tarascon, 2008). Improving the power and energy density of LIBs and reducing their unit price per kilowatt-hour remain a challenge and continue to be a subject of intensive research efforts.

LIBs are composed of three main components: a positive (cathode) and a negative (anode) electrode and electrolyte. During the LIB's charging/discharging process, Li^+ ions travel through the electrolyte between the cathode and the anode. Due to their structural stability and high energy density (Nitta *et al.*, 2015), $LiMO_x$ (M = Mn, Co, Ni, *etc.*) compounds are preferred for the cathode material. The anodes are usually made of carbon-based materials (graphite, hard carbon, *etc.*), because they provide high power and capacity with relatively

low cost (Xu *et al.*, 2013; Wu *et al.*, 2002). While the primary purpose of the electrodes is to host Li⁺ ions during charge/discharge cycles of the battery, the ionic conductivity is facilitated by the electrolyte. In order to prevent electrical short circuits during charge/discharge cycles, the ionically conductive electrolyte must be electrically insulating.

There are many different types of electrolytes used in LIBs (non-aqueous electrolytes, aqueous solutions, ionic liquids, polymer electrolytes, hybrid electrolytes, *etc.*), each with unique advantages for various targeted properties like high ionic conductivity, high boiling point and low chemical activity. The most sought-after characteristics of electrolytes are high ionic conductivity, low viscosity, low melting point, non-toxicity, low cost and recyclability, which are optimized by mixing several ingredients like solvents, salts and other additives (Liu *et al.*, 2016, 2017; Ek *et al.*, 2017).

Careful choice of solvents, the type and concentration of salts and inclusion or exclusion of further electrolyte additives determines the overall battery performance (Aurbach *et al.*, 2004; Zhang, Jow *et al.*, 2002; Aurbach *et al.*, 2007). A non-aqueous organic electrolyte that acts as an ionic path between two electrodes is formed by dissolving electrolyte salts such as LiPF$_6$, LiBF$_4$, LiClO$_4$ in a solvent mixture of alkyl carbonates including ethylene-, dimethyl-, diethyl-, ethyl methyl-, propylene- carbonates (EC, DMC, DEC, EMC, PC, respectively). The alkyl carbonates are chosen as electrolyte solvents due to their advantageous electrochemical (anodic stability, polarity), physical (wide liquid range) and safety (low toxicity) features (Aurbach *et al.*, 2004). LIB electrolytes mostly involve solvent mixtures with high permittivity (such as EC) and low viscosity linear carbonates (such as DMC, DEC) in order to simultaneously promote ionic dissociation and ion mobility. The optimum electrolyte often requires fine-tuning the charge carrier density by adjusting the salt concentration (Zhang, Jow *et al.*, 2002; Aurbach *et al.*, 2004, 2007; Xu, 2004).

The ionic conductivity of electrolytes is expected to be high enough to minimize the internal resistance of the battery (Xu, 2004). In non-aqueous solvents based on mixed alkyl carbonates, among other salts, LiPF$_6$ results in a relatively high conductivity and forms a good solid electrolyte interphase (SEI) when dissolved in EC–DMC or PC–EC–DMC electrolytes. Electrolyte additives such as LiBC$_4$O$_8$ (LiBOB) and C$_4$H$_{10}$O$_3$S are used to improve the cyclability of LIBs. LiBOB has received significant attention as an additive since it forms a SEI film with superior thermal stability and better performance concerning safety (Xu *et al.*, 2002, 2005; Panitz *et al.*, 2006; Jiang & Dahn, 2003). The SEI film, typically around 20–50 nm thick, forms on the surface of the electrodes during the initial charging of the battery as a result of the decomposition of the solvent and/or electrolyte. It prevents further breakdown of the electrolyte solution and improves cycling performance and stability of LIBs (Nie *et al.*, 2013; Ganesh *et al.*, 2012). Additionally, the choice of the electrolyte determines the dissolution and mobility of Li⁺ ions, which are key parameters in the overall LIB performance (Johansson, 2007). Therefore, a comprehensive knowledge of the electronic structure of the electrolyte and the reaction channels forming

the SEI is of great importance in LIB design that would potentially lead to better performing LIBs.

We utilized X-ray Raman scattering (XRS) spectroscopy to study the element-specific electronic structure of LIB electrolyte solutions. The present manuscript demonstrates the application of XRS on ethylene carbonate–dimethyl carbonate (EC:DMC) and propylene carbonate (PC) solvents with various salt concentrations and the presence of additive. XRS is a photon-in/photon-out technique, where a hard X-ray photon inelastically scatters from a core-level electron, promoting the electron to an unoccupied valence level. The method provides information on the electronic structure and the local chemistry of the host ion similar to X-ray absorption spectroscopy (Soininen *et al.*, 2005; Inkinen *et al.*, 2014; Juurinen *et al.*, 2013). Since both the incoming and outgoing photons are in the hard X-ray regime (typically ∼10 keV), XRS spectroscopy is a more versatile alternative to more commonly used methods like X-ray photoelectron spectroscopy (XPS) (Andersson *et al.*, 2004; Veith *et al.*, 2011; Unger *et al.*, 2017), electron energy-loss spectroscopy (EELS) (Graetz *et al.*, 2003; Tan *et al.*, 2012) and X-ray absorption spectroscopy (XAS) (Fabian *et al.*, 1971; de Groot & Kotani, 2008). XRS spectroscopy enjoys clear advantages over these conventional methods in studying samples that require complex sample environments like high-pressure cells as well as liquid samples, since it is compatible with equipment such as diamond anvil cells, flow cells, furnaces and *in situ* chambers (Bergmann *et al.*, 2002a,b; Meng *et al.*, 2004; Tohji & Udagawa, 1989; Schülke, 2007; Winter & Faubel, 2006). Moreover, soft X-ray methods may fall short in probing bulk properties and become more prone to surface contaminations (Ishii *et al.*, 2011) due to their relatively lower penetrating power, which might be an advantage in investigating surface and near-surface regions (Balasubramanian *et al.*, 2007; Fister *et al.*, 2011). For instance, the chemical shift in X-ray spectra obtained with soft XAS and XRS spectroscopy suggests different oxidation states of Mn at or near the cathode surface when compared with the bulk of the cathode (Braun *et al.*, 2002). Consequently, XRS spectroscopy stands out as a viable alternative for *in situ* and *in operando* studies of LIB cells (Pascal *et al.*, 2014; Braun *et al.*, 2015).

In the present work, we demonstrate the strength of XRS spectroscopy by measuring the C and O *K*-edges of commonly used LIB electrolyte solutions and compare them with soft XAS results available in the literature (Smith *et al.*, 2014). We observe spectral shifts at both C and O *K*-edges by varying ionic concentrations and report the effects of different salts.

2. Experimental details

Electrolyte salts of LiBOB and LiPF$_6$ (98%) and anhydrous solvents of EC (99%), DMC (≥99%) and PC (99.7%) were purchased from Sigma Aldrich and stored in an argon-filled glove box until they were used. LIB electrolyte solutions were prepared by dissolving 1 *M* and 2 *M* LiPF$_6$ salts in a binary solvent of EC:DMC (1:1 vol.) and in pure PC, 1 *M* LiBOB in EC:DMC (1:1 vol.) and 1 *M* (LiPF$_6$, 5 wt% LiBOB) in

EC:DMC (1:1 vol.). Pure solvents of EC:DMC (1:1 vol.) and PC were also used for the measurements. To avoid any possible radiation damage and protect the samples from the air atmosphere, the liquid samples were filled into the hermetically sealed closed-circle flow cell with a capillary of ~1.5 mm diameter. Two different closed-circle flow cells, one designed at beamline ID20/ESRF (Sahle, Henriquet *et al.*, 2015) and one at beamline P01/PETRAIII, were used for the air-sensitive liquid sample measurements. A sample cell made out of Kapton tubing with the volume of 8 ml was used at beamline P01 (Fig. 1). The solutions were freshly prepared on site and all the sample preparation process was carried out in the glove box.

XRS studies were carried out at beamlines ID20/ESRF (Sahle, Mirone *et al.*, 2015; Huotari *et al.*, 2017) and P01/PETRAIII (Fig. 1). For both beamlines, radiation was focused to a ~10 μm (V) × 20 μm (H) spot on the sample using a Kirkpatrick–Baez mirror system leading to a photon flux density of about 10^{13} photons s^{-1}. The elastic energy was set to 9.69 keV with spherically bent back-scattering Si (660) analyzer crystals. Inelastically scattered photons were analyzed using 36 analyzer crystals at ID20 and 12 analyzers at P01. XRS measurements with a total energy resolution of ~0.8 eV at both beamlines were performed by scanning the energy of the incident beam. The data were recorded by an area detector based on Medipix chips with 55 μm × 55 μm pixel size. All measurements were carried out at room temperature. In order to minimize the Compton scattering background, the measurements were performed in a low-q regime with momentum transfers of (2.5 ± 0.6) A^{-1} for P01 and (2.9 ± 0.9) A^{-1} for ID20. As a standard procedure, the Compton contribution to the total IXS signal has been subtracted as a smooth background. Spectra of pure PC, 1 *M*

LiPF$_6$ in PC, pure EC:DMC, 1 *M* and 2 *M* LiPF$_6$ in EC:DMC were measured at beamline ID20, and 2 *M* LiPF$_6$ in PC, 1 *M* LiBOB in EC:DMC, 1 *M* (LiPF$_6$, 5 wt% LiBOB) in EC:DMC were measured at beamline P01.

In principle, XRS is a self-calibrating technique, as the elastic line is recorded before each spectrum scan. But there are sources of uncertainty, when chemical shifts of the order of a few tens of meV are to be determined and compared across two XRS beamlines. The reproducibility of the energy transfer scale for each scan at a given beamline is guaranteed by reliably determining E_0 as the center of the elastic lines for each analyzer. We measured this uncertainty to be below 10 meV by comparing several scans of pure PC at both beamlines.

Additionally, in order to assess the cross-compatibility of the beamlines, we measured pure PC under the same conditions at both P01 and ID20. Due to the non-linearity of the monochromators over the scanning range of 550 eV, we found systematic and reproducible shifts for the carbon and oxygen K-edges spectra. We remedied this cross-compatibility issue by applying a 0.2 eV shift towards the higher energy transfer region for all the O K-edge spectra and applying a 0.08 eV shift towards the lower energy transfer region for the C K-edge spectra of the samples which were measured at P01. For data treatment, the same software was used (Sahle, Mirone *et al.*, 2015; Sahle *et al.*, 2017).

3. Results and discussion

The C and O K-edges spectra for each electrolyte solution are presented in Figs. 2–5. The influence of varying concentrations of Li$^+$ ions and the presence of LiBOB additive on the solvent electronic structure can be observed through the insets of each graph. The peak positions fitted by using Gaussian functions are shown with corresponding arrows in each inset. In Fig. 6, energy shifts as a function of salt concentration in different solvents for the C and O K-edges are presented. The results are also compared with previously reported soft XAS measurements (Smith *et al.*, 2014) for increasing concentrations of LiBF$_4$ in PC.

All the C K-edge spectra of the solutions exhibit a sharp resonance between 290.5 eV and 290.6 eV resulting from the 1s–π* transition. The feature above 293 eV is assigned to the 1s–σ* transition. Considering the 1s–π* feature in greater detail [inset (*b*) of Fig. 2], the addition of 1 *M* and 2 *M* LiPF$_6$ salt shifts the peak by 0.04 eV and 0.08 eV relative to pure PC, respectively. Closer inspection of Fig. 3 [inset (*b*)] indicates that, when the solvent of EC:DMC is used, the observed shifts are 0.07 eV and 0.12 eV for 1 *M* and 2 *M* LiPF$_6$ salt additions. While 1 *M* LiBOB leads to a shift of 0.03 eV, the presence of 5 wt% LiBOB with LiPF$_6$ leads to a shift of 0.06 eV in the solvent of EC:DMC. When different salts with the same molarity are compared, 1 *M* LiPF$_6$ has a stronger effect on the shift than 1 *M* LiBOB. The same molarities of LiPF$_6$ salt cause a bigger shift in the EC:DMC solvent (Fig. 6).

As a first approximation, the positive shift in the spectral position of an absorption edge can be attributed to a higher
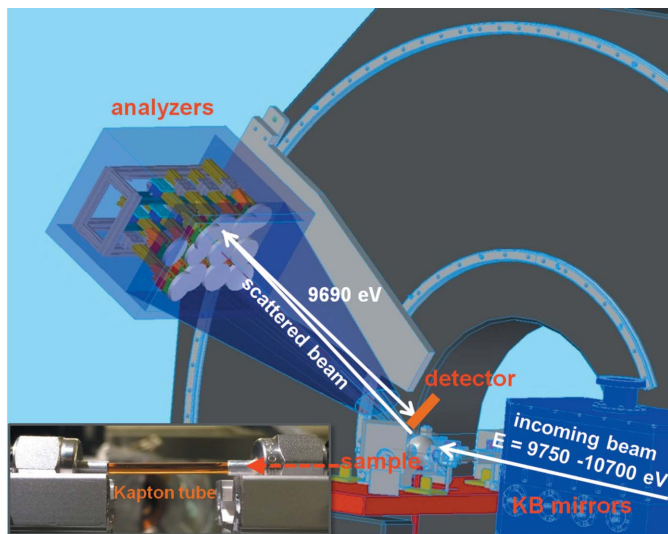

Figure 1
P01 spectrometer geometry with a photographic view of the flow cell. The incoming photon beam (from the right-hand side) is focused on the sample flow cell by the Kirkpatrick–Baez (KB) mirrors. The scattered beam is collected and focused on the detector by curved silicon crystal analysers in the forward direction. The flow cell reduces/eliminates radiation damage by replacing the sample continuously.
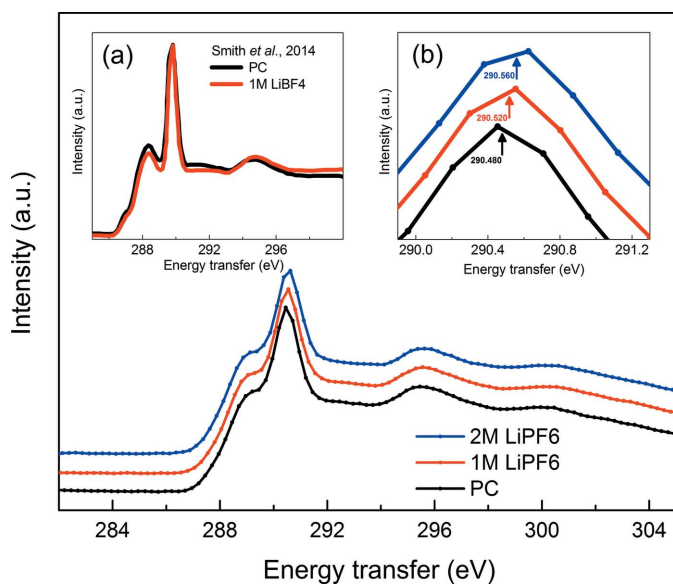
Figure 2
C K-edge XRS spectra of pure PC, 1 M and 2 M LiPF$_6$ solutions in PC. (*a*) X-ray near-edge absorption spectroscopy (XANES) data reproduced from Smith *et al.* (2014). (*b*) The inset shows the fitted peak positions with corresponding arrows.

Figure 4
O K-edge spectra of pure PC, 1 M and 2 M LiPF$_6$ solutions in PC. (*a*) 1 M LiBF$_4$ solution in PC and pure PC, as a reference reproduced from Smith *et al.* (2014). (*b*) The inset shows the fitted peak positions with corresponding arrows.

valency of the absorbing atom. In this case, the solvent molecules in EC:DMC host more positive charge than those in PC for equal molarity of LiPF$_6$. This may result in weaker van der Waals forces between Li$^+$ ions and the solvent molecules, resulting in higher ionic conductivity of LiPF$_6$ in EC:DMC when compared with LiPF$_6$ in PC. This interpretation is consistent with the conductivity measurements reported as 10.7 mS cm^{-1} and 5.1 mS cm^{-1} for these electrolyte solutions (Zhao *et al.*, 2014; Dahbi *et al.*, 2011). Additionally, considering
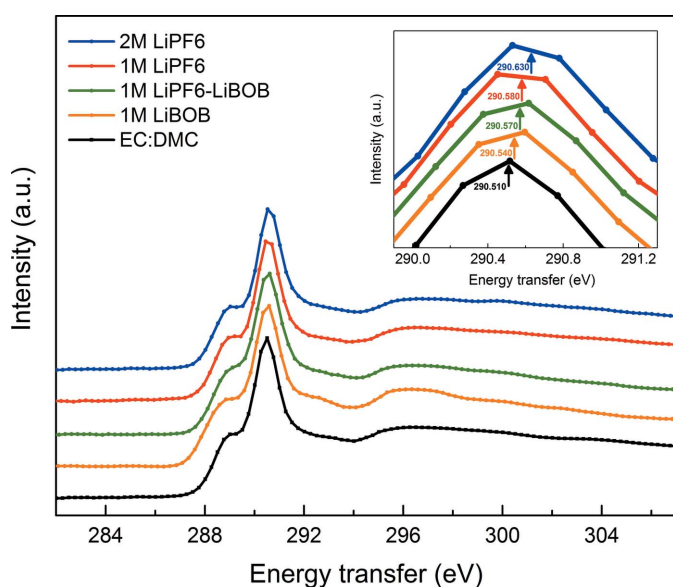
that LiBOB in EC:EMC exhibits lower ionic conductivity compared with LiPF$_6$ in EC:EMC further supports this interpretation (Wan *et al.*, 2015) with both C and O K-edges being higher for the latter (Fig. 6).

While the soft XAS measurements could not detect any significant change in the C K-edge spectra upon addition of LiBF$_4$ salt in PC (Smith *et al.*, 2014), XRS measurements showed a systematic shift for increasing LiPF$_6$ concentration in both PC and EC:DMC. It should be noted that the LiBF$_4$ salt leads to lower ionic conductivity compared with LiPF$_6$ (Zhang, Xu *et al.*, 2002; Zhang *et al.*, 2003), which might be the

Figure 3
C K-edge spectra of pure EC:DMC, 1 M LiBOB solution in EC:DMC, 1 M (LiPF$_6$, 5 wt% LiBOB) solution in EC:DMC, 1 M and 2 M LiPF$_6$ solution in EC:DMC. The inset shows the fitted peak positions with corresponding arrows.
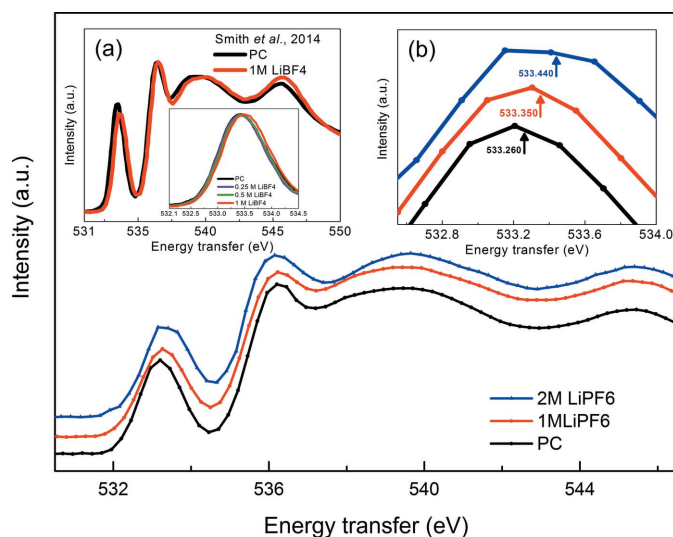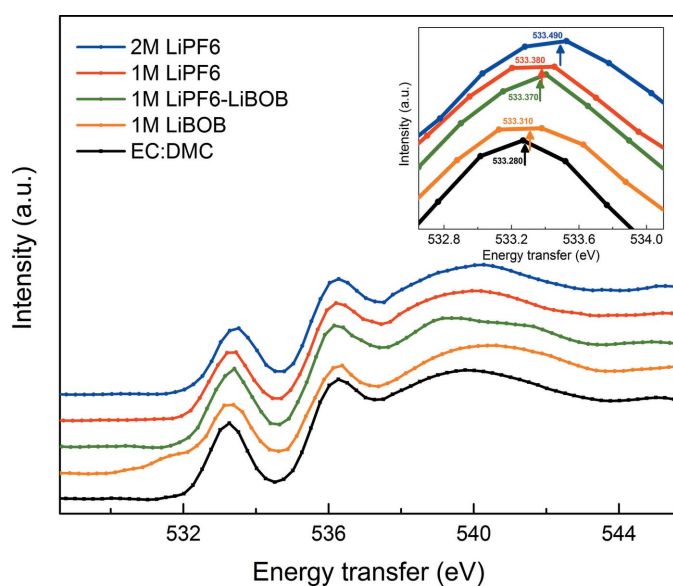

Figure 5
O K-edge spectra of pure EC:DMC, 1 M LiBOB solution in EC:DMC, 1 M (LiPF$_6$, 5 wt% LiBOB) solution in EC:DMC, 1 M and 2 M LiPF$_6$ solutions in EC:DMC. The inset shows the fitted peak positions with corresponding arrows.
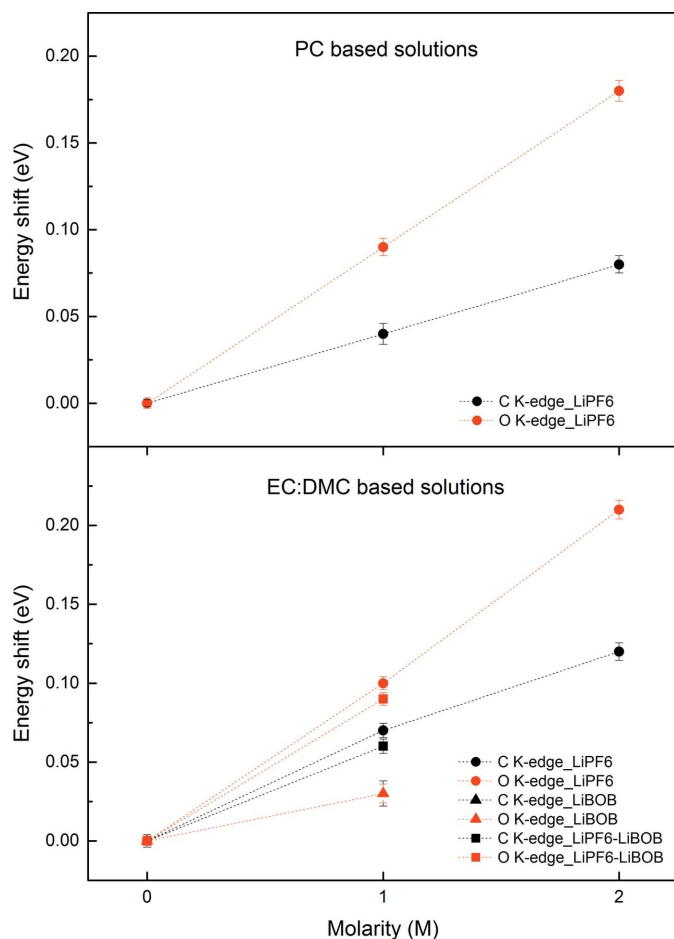
Figure 6
Energy shifts as a function of salt concentration in different solutions for the C and O K-edges.

reason for the spectral shift that we observed. Further studies with systematic comparisons might further elucidate the discrepancy.

In the O K-edge spectra of solvents and their solutions with lithium salts (Figs. 4 and 5), the first and second sharp peaks near 533 eV and 536 eV are assigned to transitions from the carbonyl and ring oxygen atoms to the π-antibonding system (π^*), respectively. $1s$–σ^* transitions from both carbonyl and ring oxygen atoms contribute to the broader third and fourth peaks in the same spectra. Among these features, only the carbonyl $1s$–π^* transition near 533 eV exhibits an energy shift upon addition of lithium salt and the presence of the additive. Increasing the lithium salt concentration does not affect the transitions from the ring oxygen atoms. Closer inspection on the carbonyl π^* peak (inset of Fig. 4) reveals that the energy shifts are 0.06 eV and 0.18 eV with the addition of 1 M and 2 M $LiPF_6$ with respect to pure PC, respectively. The inset of Fig. 5 shows that the carbonyl π^* peak shifts by 0.1 eV for 1 M $LiPF_6$ and by 0.21 eV for 2 M $LiPF_6$ relative to EC:DMC. 1 M LiBOB with a shift of 0.03 eV and 5 wt% LiBOB addition with a shift of 0.09 eV relative to EC:DMC causes weaker shifts compared with 1 M $LiPF_6$ in EC:DMC. The same concentration of different salts in EC:DMC results in the different amount of shifts on the carbonyl π^* peak (Fig. 6).

When the same molarities in different solvents are considered, the shifts are bigger in EC:DMC. Our O K-edge spectra exhibit similar spectral features to that of Smith *et al.* (2014) which shows that the carbonyl π^* feature increases as a function of concentration: 0.25 M, 0.02 eV; 0.5 M, 0.04 eV; 1.0 M, 0.07 eV relative to neat PC [inset (*a*) of Fig. 4].

4. Conclusion

Different mixtures of LIB electrolyte solutions were investigated using the X-ray Raman scattering method with the help of a closed-circle flow cell. C and O K-edges XRS spectra were collected to investigate the influence of increasing Li^+ ions and the presence of the additive on the solvent electronic structure. Our results demonstrated that, as the lithium salt concentration increased, the π^* feature in the C and the carbonyl π^* feature in the O K-edges spectra shifted to higher energies. The O K-edge spectra exhibited similar features when compared with a previous soft XAS study (Smith *et al.*, 2014); unlike the reference study the C K-edge spectra showed spectral shifts, which we attributed to differing ionic conductivities of the electrolyte solutions.

Additionally, the current study provides spectral fingerprint-like information on the electronic structure of commonly used electrolyte solutions without any decomposition of the electrolyte during the charging/discharging process of a LIB. Considering the significant variation of SEI film for different organic solvents, with carbon and oxygen being the fundamental constituents, probing the electrolyte medium is of crucial importance and hence a better understanding of the electrolyte environment will lead to an enhanced battery performance. In view of the strength of XRS spectroscopy and the penetrating power of the high-energy photons involved, *in situ* and *in operando* measurements will follow the current study.

References

Andersson, K., Nikitin, A., Pettersson, L. G. M., Nilsson, A. & Ogasawara, H. (2004). *Phys. Rev. Lett.* **93**, 196101.

Armand, M. & Tarascon, J. M. (2008). *Nature (London)*, **451**, 652–657.

Aurbach, D., Markovsky, B., Salitra, G., Markevich, E., Talyossef, Y., Koltypin, M., Nazar, L., Ellis, B. & Kovacheva, D. (2007). *J. Power Sources*, **165**, 491–499.

Aurbach, D., Talyosef, Y., Markovsky, B., Markevich, E., Zinigrad, E., Asraf, L., Gnanaraj, J. S. & Kim, H. J. (2004). *Electrochim. Acta*, **50**, 247–254.

Balasubramanian, M., Johnson, C. S., Cross, J. O., Seidler, G. T., Fister, T. T., Stern, E. A., Hamner, C. & Mariager, S. O. (2007). *Appl. Phys. Lett.* **91**, 031904.

Bergmann, U., Glatzel, P. & Cramer, S. P. (2002). *Microchem. J.* **71**, 221–230.

Bergmann, U., Wernet, P., Glatzel, P., Cavalleri, M., Pettersson, L. G. M., Nilsson, A. & Cramer, S. P. (2002). *Phys. Rev. B*, **66**, 092107.

Braun, A., Nordlund, D., Song, S., Huang, T., Sokaras, D., Liu, X., Yang, W., Weng, T. & Liu, Z. (2015). *J. Electron Spectrosc. Relat. Phenom.* **200**, 257–263.

Braun, A., Wang, H., Bergmann, U., Tucker, M. C., Gu, W., Cramer, S. P. & Cairns, E. J. (2002). *J. Power Sources*, **112**, 231–235.

Dahbi, M., Ghamouss, F., Tran-Van, F., Lemordant, D. & Anouti, M. (2011). *J. Power Sources*, **196**, 9743–9750.

Dunn, B., Kamath, H. & Tarascon, J. M. (2011). *Science*, **334**, 928–935.

Ehrlich, G. M. (2002). *G. M. Handbook of Batteries*, 3rd ed. New York/London: McGraw-Hill.

Ek, G., Jeschull, F., Bowden, T. & Brandell, D. (2017). *Electrochim. Acta*, **246**, 208–212.

Fabian, D. J., Watson, L. M. & Marshall, C. A. W. (1971). *Rep. Prog. Phys.* **34**, 601–696.

Fister, T. T., Schmidt, M., Fenter, P., Johnson, C. S., Slater, M. D., Chan, M. Y. K. & Shirley, E. L. (2011). *J. Chem. Phys.* **135**, 224513.

Ganesh, P., Kent, P. R. C. & Jiang, D. (2012). *J. Phys. Chem. C*, **116**, 24476–24481.

Graetz, J., Ahn, C. C., Yazami, R. & Fultz, B. (2003). *J. Phys. Chem. B*, **107**, 2887–2891.

Groot, F. M. F. de & Kotani, A. (2008). *Core Level Spectroscopy of Solids.* New York: CRC Press.

Huotari, S., Sahle, C. J., Henriquet, C., Al-Zein, A., Martel, K., Simonelli, L., Verbeni, R., Gonzalez, H., Lagier, M.-C., Ponchut, C., Moretti Sala, M., Krisch, M. & Monaco, G. (2017). *J. Synchrotron Rad.* **24**, 521–530.

Inkinen, J., Niskanen, J., Sakko, A., Ruotsalainen, K. O., Pylkkänen, T., Galambosi, S., Hakala, M., Monaco, G., Hämäläinen, K. & Huotari, S. (2014). *J. Phys. Chem. A*, **118**, 3288–3294.

Ishii, H., Nakanishi, K., Watanabe, I., Ohta, T. & Kojima, K. (2011). *e-J. Surf. Sci. Nanotech.* **9**, 416–421.

Jiang, J. & Dahn, J. R. (2003). *Electrochem. Solid-State Lett.* **6**, A180–A182.

Johansson, P. (2007). *Phys. Chem. Chem. Phys.* **9**, 1493–1498.

Juurinen, I., Pylkkänen, T., Ruotsalainen, K. O., Sahle, C. J., Monaco, G., Hämäläinen, K., Huotari, S. & Hakala, M. (2013). *J. Phys. Chem. B*, **117**, 16506–16511.

Liu, W., Lee, S. W., Lin, D., Shi, F., Wang, S., Sendek, A. D. & Cui, Y. (2017). *Nat. Energy*, **2**, 17035.

Liu, D., Zhu, W., Feng, Z., Guerfi, A., Vijh, A. & Zaghib, K. (2016). *Mater. Sci. Eng. B*, **213**, 169–176.

Meng, Y., Mao, H., Eng, P. J., Trainor, T. P., Newville, M., Hu, M. Y., Kao, C., Shu, J., Hausermann, D. & Hemley, R. J. (2004). *Nat. Mater.* **3**, 111–114.

Nie, M., Abraham, D. P., Seo, D. M., Chen, Y., Bose, A. & Lucht, B. L. (2013). *J. Phys. Chem. C*, **117**, 25381–25389.

Nitta, N., Wu, F., Lee, J. T. & Yushin, G. (2015). *Mater. Today*, **18**, 252–264.

Panitz, J. C., Wietelmann, U., Wachtler, M., Ströbele, S. & Wohlfahrt-Mehrens, M. (2006). *J. Power Sources*, **153**, 396–401.

Pascal, T. A., Boesenberg, U., Kostecki, R., Richardson, T. J., Weng, T., Sokaras, D., Nordlund, D., McDermott, E., Moewes, A., Cabana, J. & Prendergast, D. (2014). *J. Chem. Phys.* **140**, 034107.

Sahle, C. J., Henriquet, C., Schroer, M. A., Juurinen, I., Niskanen, J. & Krisch, M. (2015). *J. Synchrotron Rad.* **22**, 1555–1558.

Sahle, Ch. J., Mirone, A., Niskanen, J., Inkinen, J., Krisch, M. & Huotari, S. (2015). *J. Synchrotron Rad.* **22**, 400–409.

Sahle, C. J., Rosa, A. D., Rossi, M., Cerantola, V., Spiekermann, G., Petitgirard, S., Jacobs, J., Huotari, S., Moretti Sala, M. & Mirone, A. (2017). *J. Synchrotron Rad.* **24**, 269–275.

Schülke, W. (2007). *Electron Dynamics by Inelastic X-ray Scattering.* Oxford University Press.

Smith, J. W., Lam, R. K., Sheardy, A. T., Shih, O., Rizzuto, A. M., Borodin, O., Harris, S. J., Prendergast, D. & Saykally, R. J. (2014). *Phys. Chem. Chem. Phys.* **16**, 23568–23575.

Soininen, J. A., Ankudinov, A. L. & Rehr, J. J. (2005). *Phys. Rev. B*, **72**, 045136.

Tan, H., Verbeeck, J., Abakumov, A. & Van Tendeloo, G. (2012). *Ultramicroscopy*, **116**, 24–33.

Tohji, K. & Udagawa, Y. (1989). *Phys. Rev. B*, **39**, 7590–7594.

Unger, I., Seidel, R., Thürmer, S., Pohl, M. N., Aziz, E. F., Cederbaum, L. S., Muchová, E., Slavíček, P., Winter, B. & Kryzhevoi, N. V. (2017). *Nat. Chem.* **9**, 708–714.

Veith, G. M., Dudney, N. J., Howe, J. & Nanda, J. (2011). *J. Phys. Chem. C*, **115**, 14325–14333.

Wan, S., Jiang, X., Guo, B., Dai, S., Goodenough, J. B. & Sun, X. (2015). *Chem. Commun.* **51**, 9817–9820.

Winter, B. & Faubel, M. (2006). *Chem. Rev.* **106**, 1176–1211.

Wu, Y.P., Wan, C., Jiang, C. & Fang, S.B. (2002). *Principles, Introduction and Advances of Lithium Secondary Batteries.* Beijing: Tsinghua University Press.

Xu, C., Xu, B., Gu, Y., Xiong, Z., Sun, J. & Zhao, X. S. (2013). *Energ. Environ. Sci.* **6**, 1388–1414.

Xu, K. (2004). *Chem. Rev.* **104**, 4303–4417.

Xu, K., Zhang, S. S. & Jow, T. R. (2005). *Electrochem. Solid-State Lett.* **8**, A365–A368.

Xu, K., Zhang, S. S., Jow, T. R., Xu, W. & Angell, C. A. (2002). *Electrochem. Solid-State Lett.* **5**, A26–A29.

Yuan, L. X., Wang, Z. H., Zhang, W. X., Hu, X. L., Chen, J. T., Huang, Y. H. & Goodenough, J. B. (2011). *Energ. Environ. Sci.* **4**, 269–284.

Zhang, S. S., Jow, T. R., Amine, K. & Henriksen, G. L. (2002). *J. Power Sources*, **107**, 18–23.

Zhang, S. S., Xu, K. & Jow, T. R. (2002). *J. Electrochem. Soc.* **149**, A586–A590.

Zhang, S. S., Xu, K. & Jow, T. (2003). *J. Solid State Electrochem.* **7**, 147–151.

Zhao, H., Park, S., Shi, F., Fu, Y., Battaglia, V., Ross, P. N. Jr & Liu, G. (2014). *J. Electrochem. Soc.* **161**, A194–A200.